

Title

Probing the Reaction Pathway in $(\text{La}_{0.8}\text{Sr}_{0.2})_{0.95}\text{MnO}_{3+\delta}$ Using Libraries of Thin Film Microelectrodes

Authors

Robert E. Usiskin¹, Shingo Maruyama², Chris J. Kucharczyk¹, Ichiro Takeuchi², Sossina M. Haile^{1,3}

1. Applied Physics & Materials Science, California Institute of Technology, Pasadena, CA, United States.
2. Materials Science and Engineering, University of Maryland, College Park, MD, United States.
3. Chemical Engineering, California Institute of Technology, Pasadena, CA, United States.

Supplemental Information

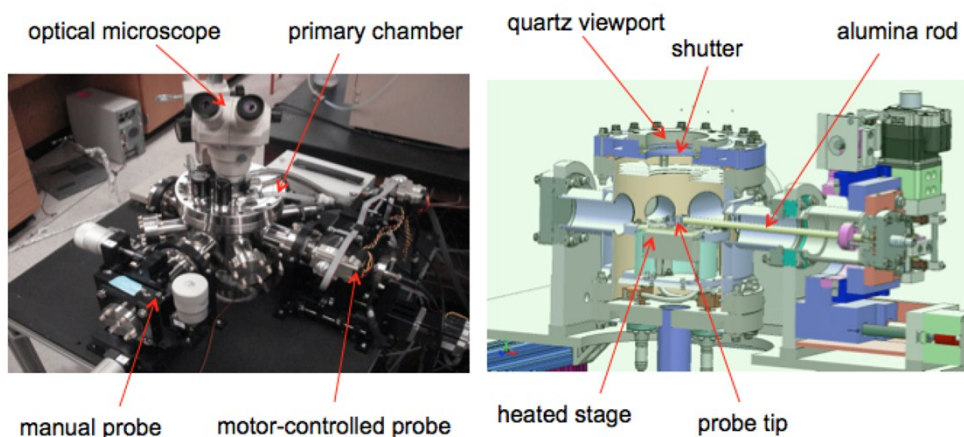


Figure S1. Primary chamber of the automated impedance microprobe used for electrochemical testing. Left: external photo. Right: computer model cross-section showing the chamber interior. For scale, the heated stage has a diameter of 5 cm.



Figure S2. Optical photograph of the asymmetric support used to heat the substrate during pulsed laser deposition of the growth temperature library, Library 2.

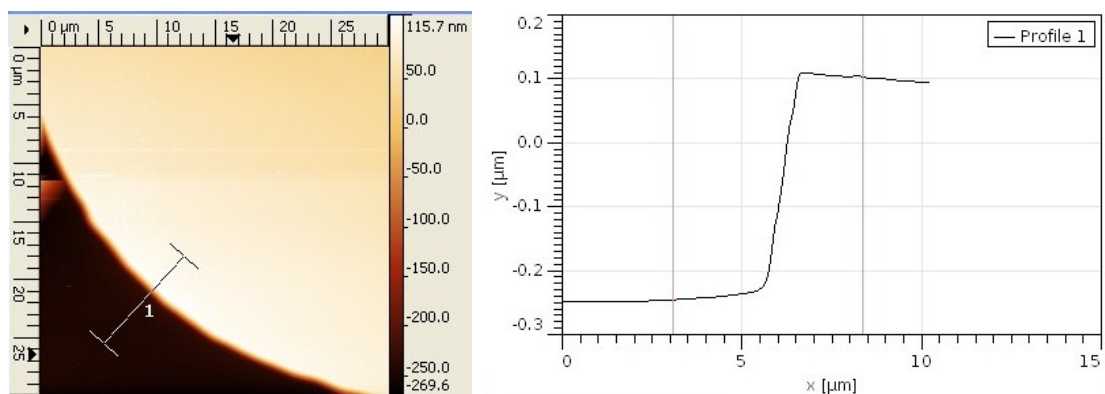


Figure S3. Typical edge profile of an LSM microelectrode prepared by dry etching. This particular profile was acquired from an 80 μm diameter microelectrode in Library 1.

Temperature calibration

Opitz and Fleig have observed¹ that in a typical microelectrode measurement the metal probe tip is cooler than the sample, and thus the probe tip cools the microelectrode by conduction during each impedance measurement. They measured that the resulting temperature drop between the counter electrode and the microelectrode can generate a Seebeck voltage of tens of millivolts, and they pointed out that the smaller the microelectrode diameter, the more the average microelectrode temperature is expected to be lowered by tip cooling. To determine an effective (average) temperature for the microelectrode, they considered an approach that uses the measured YSZ ionic conductivity and prior knowledge of the one-to-one relationship between YSZ ionic conductivity and temperature. A recent analysis indicated that this approach may be suitable for estimating the temperature at the microelectrode edge, but that it may overestimate the average temperature over the microelectrode surface.²

The current work employed a somewhat different procedure. First, a thin thermocouple was used to measure the temperature underneath the sample, i.e., the temperature of the counter electrode. This temperature closely matched the setpoint of the heated stage. Then the thermocouple was removed, and in a separate experiment, representative oxide microelectrodes of various diameters were contacted by a metal probe tip, and the induced thermovoltage $V_{\text{counter electrode}} - V_{\text{microelectrode}}$ was measured at various stage temperatures using a nanovoltmeter. The corresponding temperature drop $T_{\text{counter electrode}} - T_{\text{microelectrode}}$ was then calculated from the expression $1/\alpha \cdot (V_{\text{counter electrode}} - V_{\text{microelectrode}})$, where α is the substrate Seebeck coefficient ($\sim 0.5 \text{ mV/K}$ for YSZ³). Typical results are shown in Figure S3. From this temperature drop, the average microelectrode surface temperature was determined.

For example, with a stage temperature setpoint of 750 °C the average actual temperature of the microelectrodes under test was estimated as ranging from ~700 °C (for 100 μm diameter) up to ~720 °C (for 500 μm diameter).

In Figures 11a and 11c the deviations in the log-log relationships from the expected slope of -2.0 are attributed primarily to the temperature effects described above. Note that this tip cooling effect is not expected to significantly distort any of the other impedance trends reported in this work, since in all figures except for Figure 11, only results from 200 μm diameter microelectrodes were measured.

Upon touching the probe tip to a microelectrode, the thermovoltage typically took 5 - 180 s to stabilize, with the faster times corresponding to the higher temperatures or larger diameters. The observed thermovoltages varied slightly between measurements, and larger thermovoltages were observed when contacting metal microelectrodes than when contacting the oxide microelectrodes used in this study. These effects are likely both explained by differences in thermomechanical contact and thermal resistance at the contact point. The thermovoltages measured here are somewhat smaller than those reported by Opitz, Fleig, and their colleagues.¹ It may be that the larger stage here resulted in more radiative and convective heating of the probe, thus reducing somewhat the extent to which the probe locally cools a contacted microelectrode.

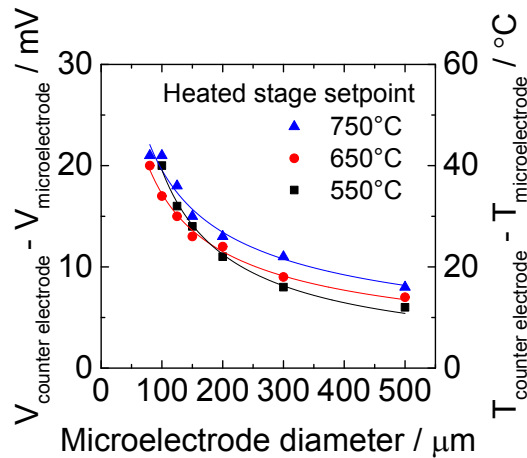


Figure S4. Seebeck voltage measured between the counter electrode and an oxide microelectrode contacted by a Paliney7 probe tip. Rescaling the voltage by the Seebeck coefficient of YSZ yields an estimate for the associated temperature drop between the electrodes, also shown. Curves are power-law fits to the data at each temperature.

Sources of uncertainty in tip position

The total error in the position of the probe tip relative to the center of the target microelectrode has several contributions with the following estimated magnitudes: creep of the Paliney7 probe tip at high temperatures ($\pm 10 \mu\text{m}$); deflection of the tip due to contact forces with the substrate ($\pm 10 \mu\text{m}$); the manual process of visually identifying reference points ($\pm 10 \mu\text{m}$); the photolithography method used to pattern the films ($\pm 5 \mu\text{m}$); and the stepper motor positioning accuracy ($\pm 1 \mu\text{m}$). The resulting total tolerance in tip position motivated the use of microelectrodes with sufficiently large diameter ($\geq 100 \mu\text{m}$) so as to ensure that reliable electrical contact could be achieved throughout the study. Probe tips made of $\text{Pt}_{0.7}\text{Ir}_{0.3}$ exhibited reduced creep and deflection but typically scratched the films at elevated temperature. Overall, it is likely possible to reduce the above tolerances in future studies and thereby reliably contact microelectrodes with smaller diameters.

Fitting routine: Choosing the initial values

Depending on the initial values chosen for the fit parameters, the fitting routine sometimes either failed to converge or converged to a solution with unreasonably large confidence intervals for all parameters. It was found that these convergence problems could largely be avoided by taking as the initial value of each fit parameter the median result for that parameter from preliminary fits to the same spectra that were performed using plausible but otherwise somewhat arbitrary initial values.

Additional Figures

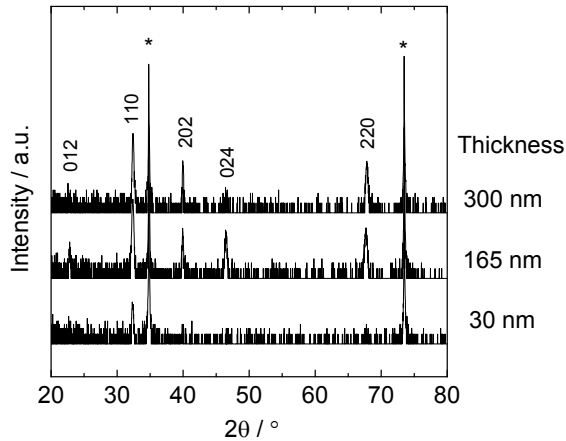


Figure S5. XRD patterns acquired from the supplemental library. The corresponding film thickness is listed to the right of each pattern. The orientation of each LSM reflection is also indicated. Reflections marked with an asterisk are from the YSZ substrate.

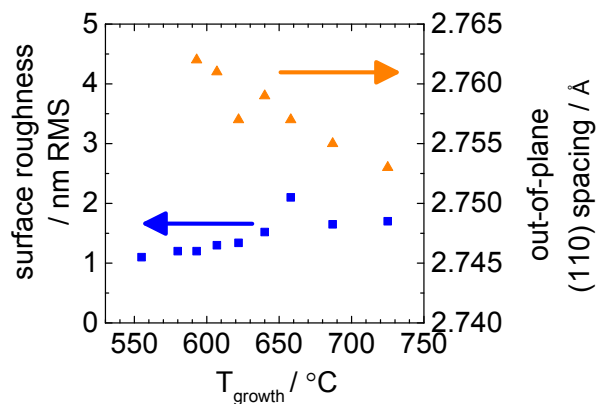


Figure S6. Surface roughness and out-of-plane (110) plane spacing measured from Library 2 using AFM and XRD, respectively.

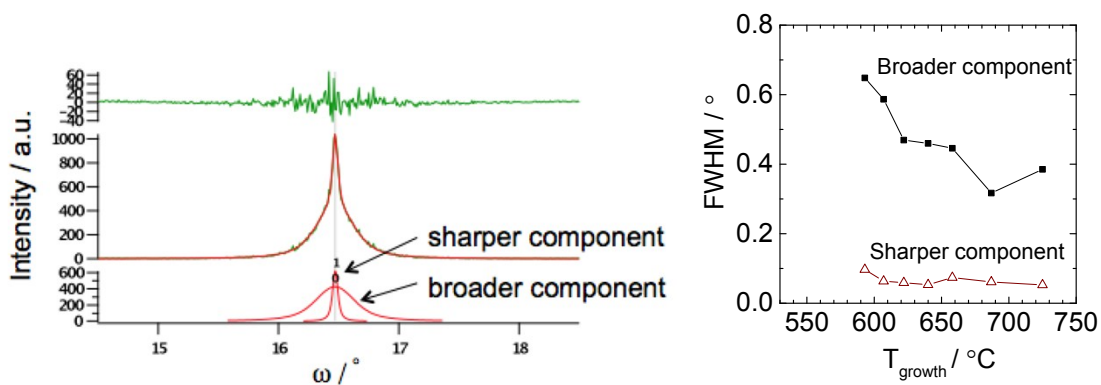


Figure S7. Typical rocking curve data acquired from Library 2. Left: Raw data and fits acquired in a region where the growth temperature was 725 °C. The two fit components are shown in red at bottom; the fit residual is shown in green at top. Right: Full width at half maximum (FWHM) values as a function of growth temperature.

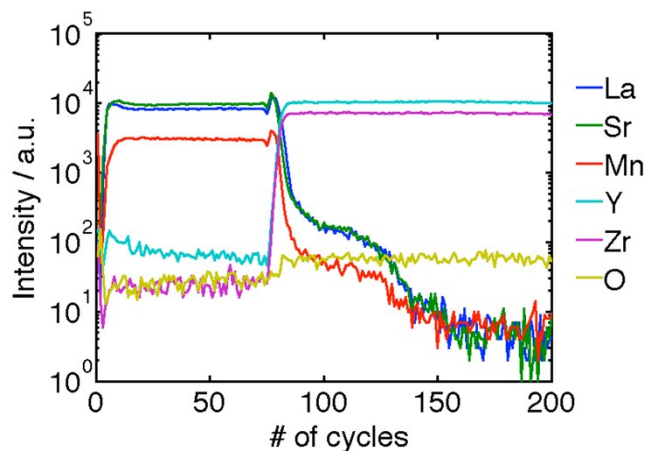


Figure S8. Secondary ion mass spectrometry measurement from a microelectrode in Library 2 grown at 627 °C.

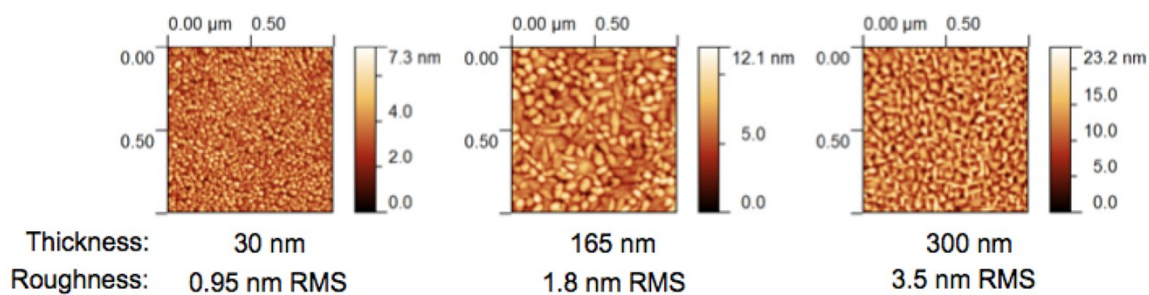


Figure S9. AFM images acquired after patterning from the supplemental library. The corresponding film thickness and root-mean-squared roughness are listed under each micrograph.

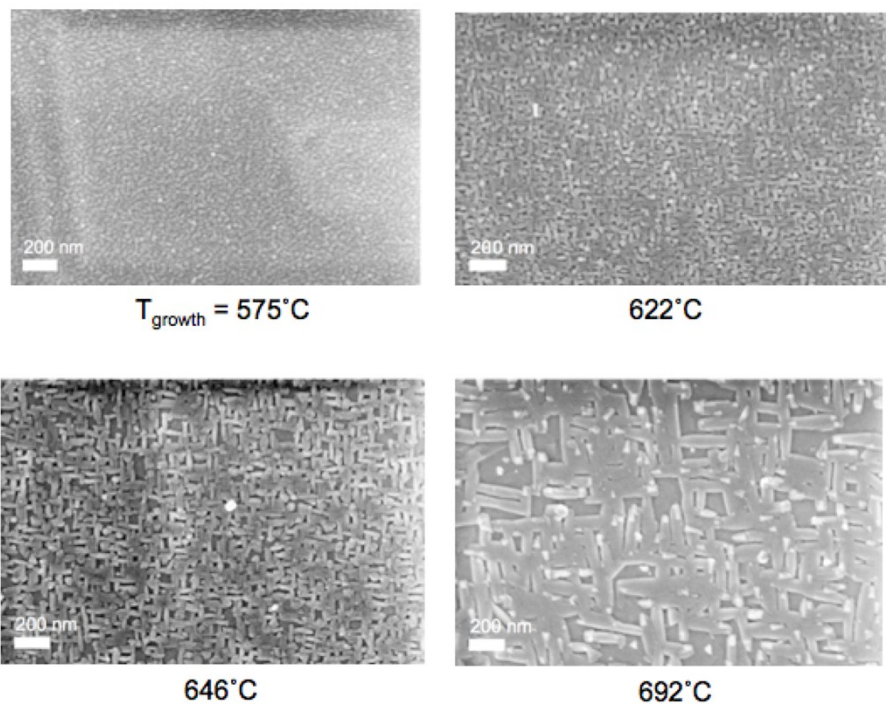


Figure S10. SEM images from Library 2 after impedance testing for 2 days at $\sim 710^{\circ}\text{C}$. Some of the observed contrast is due to mild sample charging.

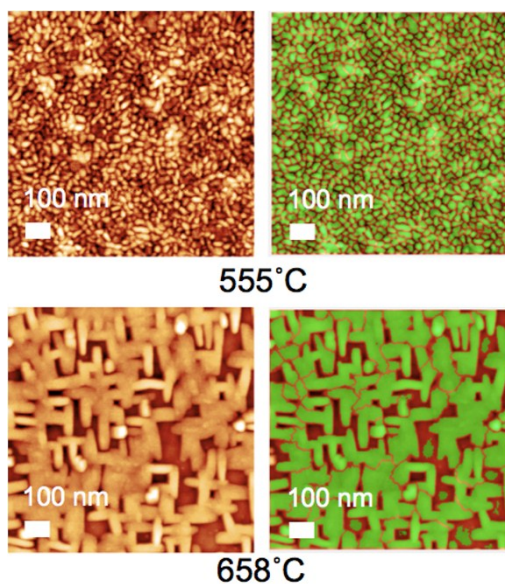


Figure S11. Typical images used to estimate the exposed grain boundary length. Films from Library 2 grown at two different temperatures are shown. Left: AFM micrographs. Right: Same micrographs after image processing. The exposed grain boundary length was estimated by summing the length of the borders between the green regions.

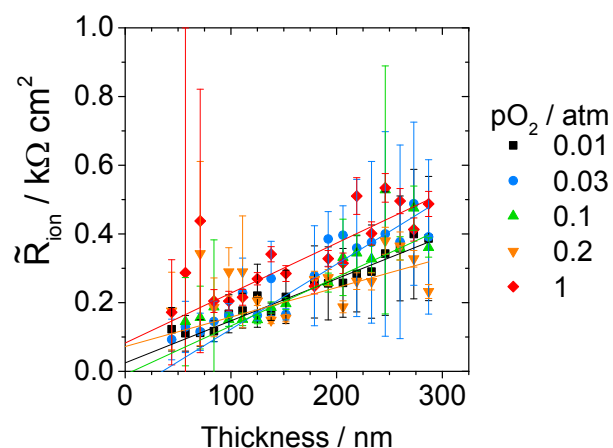


Figure S12. Thickness dependence of the bulk ionic resistance obtained from fits to impedance spectra from 200 μm diameter microelectrodes in Library 1 at $\sim 710^\circ\text{C}$ under various oxygen partial pressures as indicated. This plot is identical to Figure 13c, except here all seven parameters were free to vary in all fits, including the 0.2 atm and 1 atm fits. 95% confidence intervals are shown.

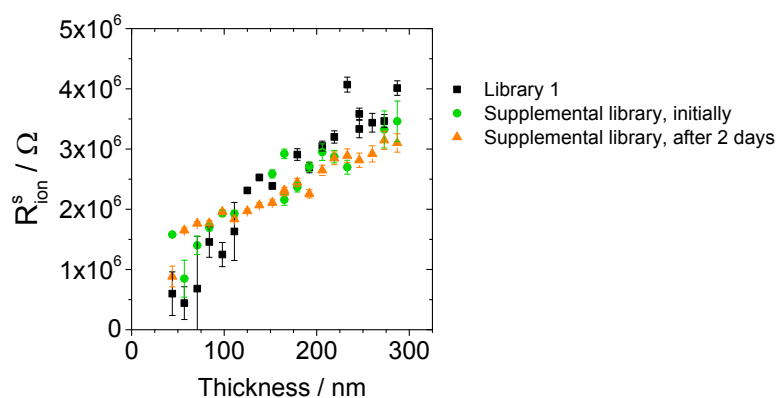


Figure S13. Surface resistance R_{ion}^s extracted from impedance spectra from both Library 1 and the supplemental library at $\sim 710^\circ\text{C}$ in 0.2 atm O_2 using 200 μm diameter microelectrodes. 95% confidence intervals are shown.

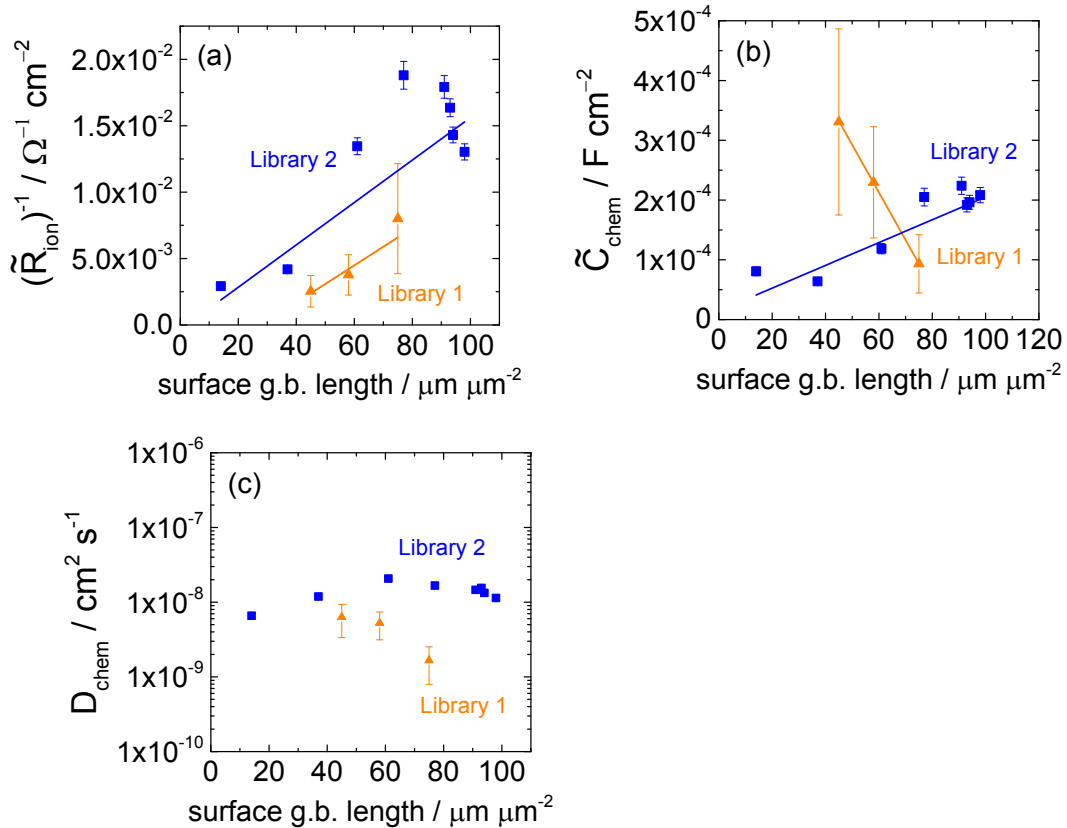


Figure S14. Dependence of bulk electrochemical parameters on surface-terminated grain boundary length as measured from 200 μm diameter microelectrodes in Libraries 1 and 2 (varied thickness for Library 1 and varied growth temperature for Library 2) under 0.01 bar O_2 ($T \sim 710 \text{ }^\circ\text{C}$). (a) through-film conductance (inverse of the through-film resistance), (b) chemical capacitance, and (c) through-film ambipolar diffusivity. All parameters are area-normalized, and 95% confidence intervals propagated from the impedance analysis are shown, except where they are smaller than the data points.

Derivation of Equation 1

An analytical expression for the equivalent impedance Z of the circuit shown in Figure 8 can be derived following the method described in the appendix of a paper by Lai and Haile.⁴ First, the circuit is recast using generalized impedance elements Z_A , Z_1 , Z_3 , and Z_D , as shown below in Figure S15. $V_1(x)$ and $I_1(x)$ are defined as the voltage and the current for the branch point in the top rail of the circuit, $V_2(x)$ and $I_2(x)$ are analogous values for the bottom rail, V_a is the input voltage, V_b is the output voltage, and I is the total current. The value of x varies from 0 at one end of the MIEC (the top face of the microelectrode) to L at the other end of the MIEC (the MIEC/YSZ interface). Additional definitions are that there are N branch points, $Z_1^{Total} = Z_1 N$, $Z_3^{Total} = Z_3 / N$, and $dx = L/N$.

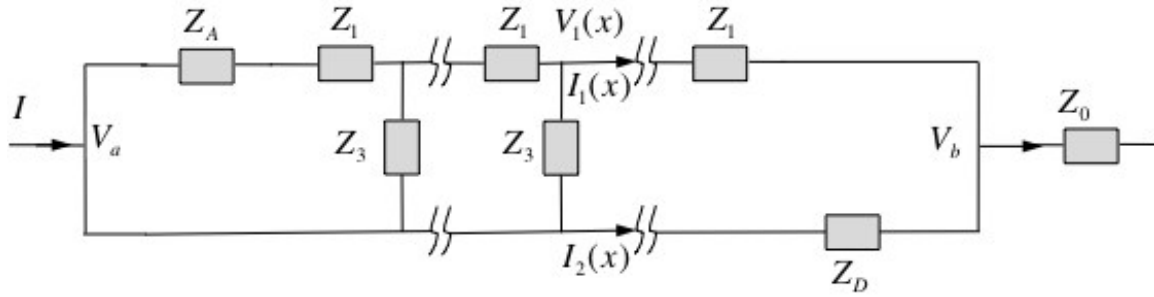


Figure S15. Generalized circuit.

From these definitions it follows that

$$Z_1 = Z_1^{Total} \frac{dx}{L} \quad (2)$$

$$Z_3 = Z_3^{Total} \frac{L}{dx} \quad (3)$$

Ohm's law implies

$$\frac{dV_1(x)}{dx} = -\frac{Z_1^{Total}}{L} I_1(x) \quad (4)$$

Kirchoff's law implies

$$-\frac{dI_1(x)}{dx} = \frac{dI_2(x)}{dx} = \frac{V_1(x) - V_a}{Z_3^{Total} L} \quad (5)$$

$$I = I_1(x) + I_2(x) \quad (6)$$

The boundary conditions are

$$V_a - V_1(0) = Z_A I_1(0) \quad (7)$$

$$V_1(L) - V_b = 0 \quad (8)$$

$$V_a - V_b = Z_D I_2(L) = ZI \quad (9)$$

From equations 4 - 5, one obtains

$$Z_3^{Total} L^2 I_1'' - Z_1^{Total} I_1 = 0 \quad (10)$$

The solution to equation 10 is

$$I_1(x) = C_1 e^{kx} + C_2 e^{-kx} \quad (11)$$

with

$$k = \sqrt{\frac{Z_1^{Total}}{L^2 Z_3^{Total}}} \quad (12)$$

The solutions to the other parameters are

$$I_2(x) = -C_1 e^{kx} - C_2 e^{-kx} \quad (13)$$

$$V_1(x) = -\frac{Z_1^{Total}}{L} \left[\frac{C_1}{k} e^{kx} - \frac{C_2}{k} e^{-kx} \right] \quad (14)$$

Applying the boundary conditions, the desired expression is obtained:

$$Z = \frac{R_{ion} Z_D + Z_A Z_D kL * \coth(kL)}{R_{ion} + \frac{Z_A Z_D (kL)^2}{R_{ion}} + (Z_A + Z_D) kL * \coth(kL)} \quad (15)$$

where the generalized impedance elements are defined as

$$Z_3^{Total} = \frac{1}{j\omega C_{chem}} \quad (17)$$

$$Z_D = \frac{1}{j\omega C_{eon}^\perp} \quad (18)$$

$$Z_A = \frac{R_{ion}^s}{1 + R_{ion}^s Y_{ion}^s (j\omega)^n} \quad (19)$$

and the argument of the coth can be evaluated from equation 12 to obtain

$$kL = \sqrt{j\omega R_{ion} C_{chem}} \quad (20)$$

Supplemental references

- 1 Opitz, A. K. & Fleig, J. Investigation of O-2 reduction on Pt/YSZ by means of thin film microelectrodes: The geometry dependence of the electrode impedance. *Solid State Ion.* **181**, 684-693, doi:Doi 10.1016/J.Ssi.2010.03.017 (2010).
- 2 Huber, T. M., Opitz, A. K., Kubicek, M., Hutter, H. & Fleig, J. Temperature gradients in microelectrode measurements: Relevance and solutions for studies of SOFC electrode materials. *Solid State Ion.* **268**, 82-93, doi:10.1016/j.ssi.2014.10.002 (2014).
- 3 Ahlgren, E. O. & Poulsen, F. W. Thermoelectric power of stabilized zirconia. *Solid State Ion.* **82**, 193-201, doi:Doi 10.1016/0167-2738(95)00201-3 (1995).
- 4 Lai, W. & Haile, S. M. Impedance Spectroscopy as a Tool for Chemical and Electrochemical Analysis of Mixed Conductors: A Case Study of Ceria. *J American Ceramic Society* **88**, 2979-2997, doi:10.1111/j.1551-2916.2005.00740.x (2005).